

Influence of boron implantation induced defects on solar cells: Modeling the process defects

Cite as: J. Appl. Phys. 133, 065703 (2023); doi: [10.1063/5.0130315](https://doi.org/10.1063/5.0130315)

Submitted: 11 October 2022 · Accepted: 26 January 2023 ·

Published Online: 14 February 2023



[View Online](#)



[Export Citation](#)



[CrossMark](#)

Sangaravadi Vel Masilamani,¹ Ramachandran Ammapet Vijayan,² and Muthubalan Varadharajaperumal^{1,a}

AFFILIATIONS

¹104, Device Modeling Lab, ASK-II, SASTRA Deemed University, Thanjavur, Tamil Nadu 613 401, India

²Amrita School of Engineering, Amrita Vishwa Vidyapeetham, Chennai Campus, Vengal Village, Thiruvallur 601 103, Tamil Nadu, India

^aAuthor to whom correspondence should be addressed: muthubalan@ece.sastra.edu

ABSTRACT

The effect of process-induced defects on the photo-generated charge-carrier lifetime and solar cell performance is critical, which will help optimize the process recipe. In this work, we attempt to quantify the effects of process-induced defects during boron implantation on the n-type silicon wafer in different annealing ambiances. We have evaluated the role of defects that can be formed during oxygen and inert ambience annealing on n-type bifacial passivated emitter rear totally diffused solar cells using a recombination current prefactor (J_0). The numerically calculated J_0 is calibrated with the reported experimental J_0 values using two different methods: (i) Shockley–Read–Hall lifetime and (ii) effective trap-density method. In the latter method, we used the simulated defect density profiles. Both methods capture the process-induced degradation. We observed that the process-induced defects could deteriorate by almost 1% absolute efficiency for the considered annealing conditions. We found that dislocation loops alone cause an ignorable effect on terminal characteristics, but other process-induced mechanisms could dominantly degrade the cell's performance. To further support, we show that independent defects (apart from coupled defects) other than dislocation loops could explain the experimentally reported boron-implanted diodes' J–V curves under reverse bias conditions.

Published under an exclusive license by AIP Publishing. <https://doi.org/10.1063/5.0130315>

I. INTRODUCTION

The crystalline silicon (c-Si) solar cell production value chain consists of a series of interconnected, complex steps that convert the silicon wafer into solar cells. One of many critical steps is to form heavily doped regions. The doped region's functionality is to create a conductive difference,¹ which gives selective nature to the solar cell for collecting a single type of charge carrier from the photon-generated electron-hole pair. To form doped regions, ion implantation is a well-known technique due to its higher dopant uniformity and the elimination of some process steps, such as edge isolation and removal of silicate glass, which is formed during diffusion.^{2–7} Implantation with in-suit masking during fabrication makes local doping even easier by cutting down on the number of fabrication steps.^{8–10} Advances in ion beam technologies, as well as its unidirectional nature, make it a viable candidate for mass manufacturing with higher throughput.^{7,10–12}

The n-type wafer outperforms its p-type counterpart due to its better tolerance for unwanted metal impurities and boron oxygen

complexes that induce light-induced degradation (LID).^{13–16} As a result, boron implantation is an unavoidable process step in creating a conductivity difference in an n-type wafer for an implanted solar cell. Higher annealing temperatures and longer annealing times improve the cell performance by removing lattice damage caused by the implantation process.^{5,17,18} However, dislocation loops (DLs)^{19–21} and boron clusters^{17,22,23} survive and act as extrinsic defects even after high-temperature annealing. Even when boron implantation does not amorphize the silicon lattice, DLs appear when the boron dose exceeds $5 \times 10^{14} \text{ cm}^{-2}$.^{24,25}

Charge carriers that have been separated due to conductive differences must reach the respective contact without the interference of extrinsic recombination centers. Extrinsic recombination can be greatly reduced using a high-quality absorber. However, defects formed during the process have an irreversible negative effect by acting as recombination centers.^{23,26–28} Dislocation loops formed during the implantation damage annealing, in particular, act as a recombination center.^{19,29}

TABLE I. Three different annealing sequences adapted to study the effect of process-induced defects on n-PERT cells.

Annealing sequences	Step-1	Step-2	Step-3	Step-4	Step-5
Oxidation first (A1)	Ramp up to 950 °C	Annealing at 950 °C in O ₂ ambience	Ramp up to 1050 °C	Annealing at 1050 °C in N ₂ ambience	Ramp down from 1050 to 800 °C
Oxidation last (A2)	Ramp up to 1050 °C	Annealing at 1050 °C in N ₂ ambience	Ramp down to 950 °C	Annealing at 950 °C in O ₂ ambience	Ramp down to 800 °C
Inert annealing (A3)	Ramp up to 1050 °C	Annealing at 1050 °C in N ₂ ambience	Ramp down to 800 °C

Accounting for the process defects in device simulation is important to understand the effect of process-induced defects on device terminal characteristics. It is not straightforward because there is no quantitative model to account for the recombination that occurs due to the dislocation loop. Various studies' efforts to determine the effect of process-induced defects on device performance can reach the point of relating process defects to experimental or analytical J_0 .^{17,20,22,23,30,31} We successfully account for the process-induced defects from the process simulation into the device simulation by employing (i) Shockley–Read–Hall (SRH) lifetime and (ii) effective trap-density methods. Furthermore, we investigated the impact of process-induced defects on the terminal characteristics of passivated emitter rear totally diffused (PERT) solar cells.

Shockley–Read–Hall (SRH) recombination is an intriguing extrinsic recombination mechanism that occurs via intermediate energy states at forbidden gaps between bands.^{32,33} Defects that grow during the process introduce energy states into the bandgap.^{19,29} The SRH lifetime is the average time that it takes the carrier to annihilate through these energy states, and it is used to calibrate simulated J_0 with experimentally measured J_0 . In device simulation, the optimized SRH lifetime at both emitter and bulk regions accounts for the process-induced defects. In the effective trap-density method, J_0 is set by optimizing the defect density, and this is taken into account in cell-level simulation as a trap density. In Sec. II, we discuss the process simulation and its calibration. In Sec. III, we discuss the device simulation and its calibration. In Sec. IV, we discuss the annealing ambience induced defects. In Sec. V, we discuss different strategies to account for process-induced defects. In Sec. VI, we discuss the calibration of different experimental J–V data to capture the nature of the process-induced defects and their mechanism. Finally, in Sec. VII, we discuss the effect of process-induced defects on the terminal characteristics of the PERT solar cell. Despite the fact that we study implantation-induced defects, this work can be extended to any process-induced defects as well.

II. PROCESS SIMULATION AND CALIBRATION

The impression of damage, formed during the process, on device performance is studied by adapting different annealing ambiances at the implanted energy of 5 keV for three different doses: $8 \times 10^{14} \text{ cm}^{-2}$, $1.5 \times 10^{15} \text{ cm}^{-2}$, and $2 \times 10^{15} \text{ cm}^{-2}$ on a $2 \Omega \text{ cm}$ n-type c-Si wafer. The annealing ambiances are tabulated in Table I.

Boron implantation and diffusion kinetics are studied using the Sentaurus Process (SP).³⁴ The spatial distribution of implanted boron ions is calculated by means of a dual Pearson analytical model, and the damage is calculated with the Hobler model.³⁵ The resultant crystal defect was caused by boron implantation, which necessitated high-temperature annealing to rebuild the lattice and activate the dopant (>950 °C).³⁶ During annealing, the interactions of the dopant atom (B) with the host atom (Si) and the defect formation kinetics (from small interstitial clusters to dislocation loops) are accounted for using the models listed in Table II. Along with defect formation, some unwanted phenomena, such as transient enhanced diffusion (TED) and oxidation enhanced diffusion (OED), during annealing lead to enhanced dopant diffusion and dopant segregation (reducing dopant activation), which are also accounted for using respective models.

To improve the simulation reliability, we calibrated our simulation boron profiles with the experimental SIMS profile using SP models in Table II, as shown in Fig. 1. In inert annealing ambience, the diffusivity “D” of the dopant transport model, which governs the diffusion kinetics, is used to calibrate the boron distribution. In an oxygen atmosphere, D and the surface recombination parameter of the “ThreePhaseSegregation” model, which controls the segregation flux in the growing oxide layer, help match the simulation to experimental data.

III. DEVICE SIMULATION AND J_0 CALIBRATION

The Sentaurus device simulation tool⁴⁰ is used to calculate J_0 and terminal characteristics of a bifacial n-PERT solar cell. The J_0 and J–V curves are calculated using the boron profiles, which are calibrated in the SP for all three annealing sequences as given in Table I. To account for charge-carrier recombination, the Altermatt–Auger model and the SRH recombination model (doping independent) are used to calculate J_0 and J–V in device

TABLE II. Sentaurus process models.

Phenomenon	Models	Reference
Dopant transport	ChargedReact	34
Defect clusters	ChargedCluster	34
Dislocation loop	MultiClusterModel	37
Dose loss during oxidation	ThreePhaseSegregation	38 and 39

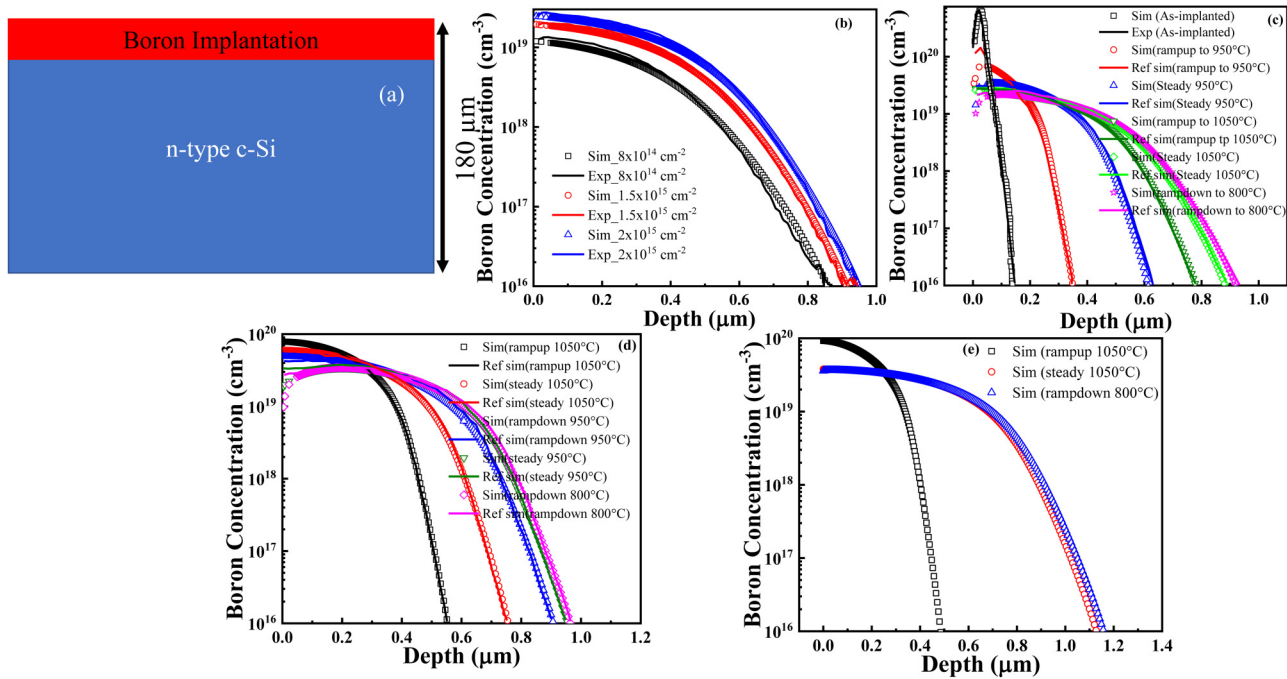


FIG. 1. (a) Schematic of boron implantation. (b) Comparison of simulation and experimental boron profiles for three different implanted doses: $8 \times 10^{14} \text{ cm}^{-2}$, $1.5 \times 10^{15} \text{ cm}^{-2}$, and $2 \times 10^{15} \text{ cm}^{-2}$. For the implanted dose of $2 \times 10^{15} \text{ cm}^{-2}$, the simulated boron profiles (symbols) during different stages of annealing sequence are shown for (c) oxidation-first, (d) oxidation-last, and (e) inert ambience, and available reported simulation data (lines) are shown in (c) and (d).

simulation. The Yan–Cuevas bandgap narrowing model (BGN) is used to account for BGN caused by dopant and excess carrier concentration.^{41,42} The surface recombination velocity (SRV) is calculated using the surface dopant concentration.⁴³

A. J_0 calibration

The recombination current density (J_0) is a lumped parameter that quantifies the total recombination losses in solar cells. It is comprised of various recombination mechanisms (radiative recombination, SRH recombination, surface SRH recombination, and Auger recombination) that take place in the bulk and on the surface.⁴⁴ It is often used to quantify the quality of the doped region of solar cells, particularly, to understand the process-induced defects in the doped region. The defects formed during the process act as recombination centers, increasing J_0 via the SRH recombination mechanism.

By taking into account the process-induced defects in device simulation, J_0 is calculated numerically and calibrated with the experimental J_0 by optimizing SRH lifetime. The test structure used to calculate J_0 is shown in Fig. 2(a). The optimized boron profiles from SP (see Fig. 1) are used in the boron implanted region of the test structure. The simulation J_0 and its components (the contributions of each recombination mechanism) are measured using dark J-V,⁴⁵ and they are validated using the online tool EDNA-2, which

is given in Fig. 2(b). The J_0 component separation is discussed in Appendix A.

IV. ANNEALING AMBIENCE INDUCED DEFECT (PROCESS PHYSICS BEHIND DEFECT FORMATION)

Annealing followed by boron implantation recovers implanted damage and activates the implanted boron ions by replacing the host atom. Along with the aforementioned advantages, defects are formed as a causal sequence of annealing that contributes to recombination. The ambience during annealing has the ability to influence dopant activation and defect growth kinetics. We investigated the dopant activation and defect growth kinetics using components (recombination mechanisms) of calibrated J_0 for three different annealing sequences (from A1 to A3, as given in Table I) in this section. The optimized SRH lifetime, which is used to calibrate the experimental J_0 , will aid in the investigation of the effects of defects on solar cell terminal characteristics (in Sec. VI).

A. Oxidation-first annealing (A1)

In the A1 process, the implanted sample is annealed in an oxygen atmosphere at 950°C as the first step of this annealing sequence. The resultant oxide layer is grown on the surface of silicon, which increases the self-interstitial (Si-atom) concentration with pre-existing interstitial defects (due to implantation) in the bulk due to volume expansion. This super-saturation point defect

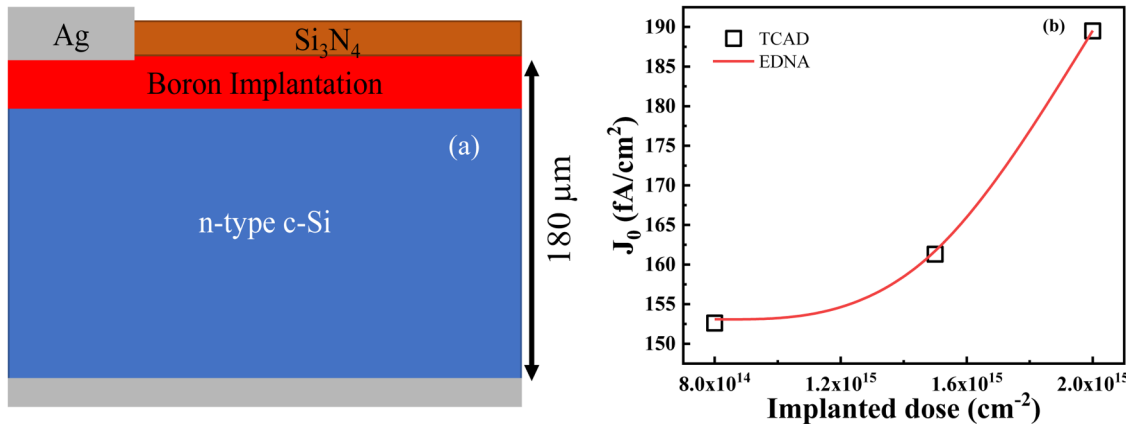


FIG. 2. (a) Schematic of the PN-junction test structure (to calculate J_0). (b) Our simulated J_0 vs EDNA-2 simulated J_0 .

concentration creates an auspicious situation to form different defects, such as small interstitial clusters and boron interstitial clusters. The small interstitial clusters will develop further into dislocation loops (DLs) through the Ostwald ripening process.^{20,36,37,46} These defects are stable even after consecutive high-temperature annealing at 1050 °C in an inert atmosphere, as evident in Fig. 3(a), and they are replicated in components of J_0 in Fig. 4(a).

Because of the enhanced defect formation caused by oxidation first in the annealing sequence, SRH recombination dominates total recombination (J_0). Surface SRH is the next dominant recombination mechanism, which depends on surface dopant concentration. The default SRV at the Si/SiO₂ interface is maintained as 1×10^4 cm/s.⁴⁷ The contribution of surface SRH to total J_0 is greater in oxidation-first annealing compared to other annealing sequences (A2 and A3), which is due to lower dopant activation ($n_p = n_i^2$), as shown in Fig. 4(b). The lower dopant activation is the effect of boron's high segregate nature, which induces boron diffusion from the silicon into the growing oxide layer during annealing. Figure 4(c) shows the segregated boron concentration in the oxide layer, which is further validated by the boron cluster concentration.

Boron cluster formation is low compared to other annealing processes, as shown in Fig. 3(a), which may be due to the relatively lower boron availability during annealing. Auger recombination is the next most important contributor to total recombination. However, the contribution of Auger to total J_0 is lower in oxidation-first annealing compared to other annealing sequences (A2 and A3), which is also due to lower dopant activation, as shown in Fig. 4(b). The radiative recombination mechanism is negligible compared to the other three recombination mechanisms.

B. Oxidation-last annealing (A2)

In the oxidation-last annealing sequence (A2), the boron implanted sample is annealed in an inert ambience at 1050 °C as the first step in this annealing sequence. Most of the interstitial concentration due to implantation starts to recombine with vacancies, and hence, the interstitial concentration reduces considerably during this high-temperature inert annealing. The temperature is ramped down to 950 °C after some annealing time from 1050 °C, and oxygen ambience is introduced instead of inert ambience.

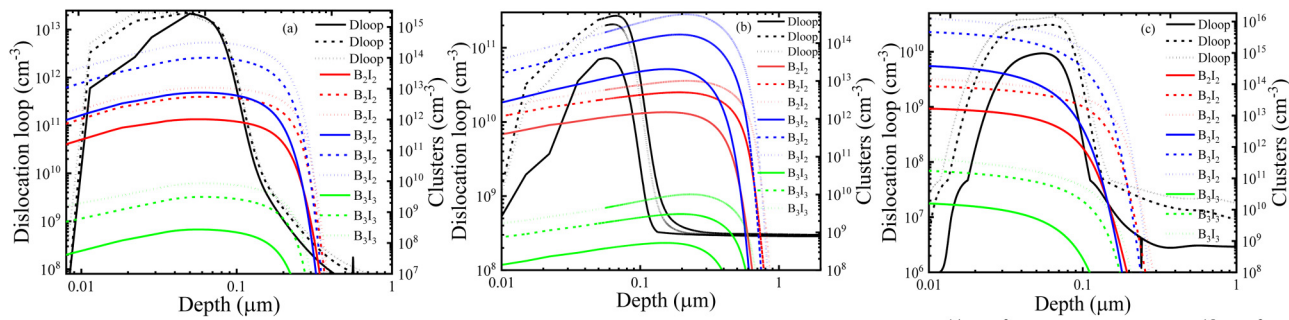


FIG. 3. Simulated profiles of DL and boron interstitial clusters for three implanted doses: 8×10^{14} cm⁻² (solid line), 1.5×10^{15} cm⁻² (dashed line), and 2×10^{15} cm⁻² (dotted line). (a) Oxidation-first annealing sequences (A1). (b) Oxidation-last annealing sequence (A2). (c) Inert annealing (A3).

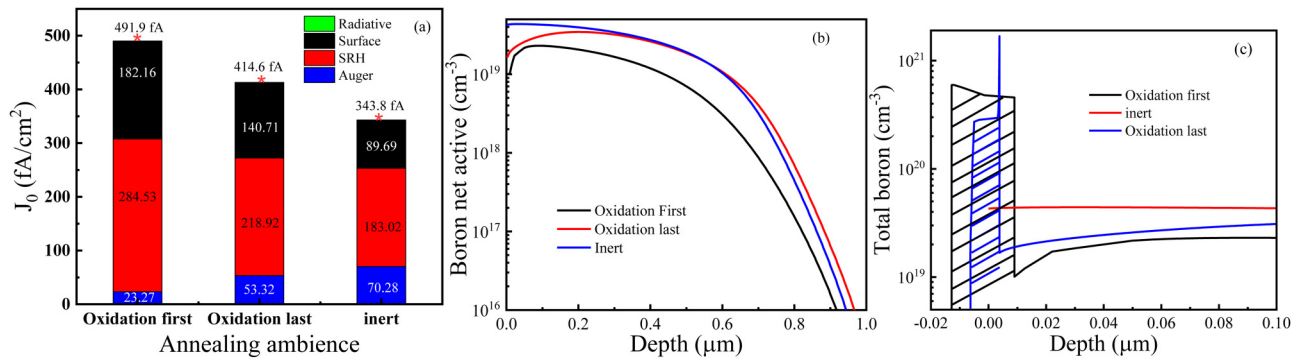


FIG. 4. (a) Separation of a J_0 component (SRH, Auger, surface SRH, and radiative) for all three annealing sequences at an implanted dose of $2 \times 10^{15} \text{ cm}^{-2}$. (b) Boron net-active concentration for all three annealing schemes at the implanted dose of $2 \times 10^{15} \text{ cm}^{-2}$. (c) Boron consumed by the oxide layer during its growth as shown in the magnified image. No oxide layer growth in inert ambient could be observed.

Besides the self-interstitial injection during the consecutive oxidation at 950°C , comparatively fewer DLS have been formed than A1 as a result of recombined implanted interstitial defects in this sequence earlier [see Fig. 3(b)]. The boron cluster concentration is increasing compared to the previous annealing sequence due to the availability of boron, which is a result of reduced boron segregation. The J_0 calibration in Fig. 4(a) shows that the SRH recombination mechanism contributes significantly to total recombination like the A1, but comparatively less than the A1.

Despite the fact that boron segregation is lower than in A1, significant surface dopant concentration is available after subsequent oxidation steps, which is reflected in J_0 . Surface SRH is the next dominant recombination mechanism, which is lower than A1 due to reduced surface dopant segregation. Auger recombination is the next dominant recombination mechanism, and its contribution to total recombination is greater than that of the A1 due to higher dopant activation. The increased dopant activation could be attributed to less boron segregation into oxide during oxygen ambience, as shown in Figs. 4(b) and 4(c). During inert ambience (the first step in this sequence), a significant amount of implanted boron diffuses into the silicon, resulting in lower boron surface concentration, which reduces boron segregation during oxidation during this annealing sequence. As a result, dopant activation increases.

C. Inert annealing (A3)

The annealing sequence changes cause significant differences in the defect formation kinetics, which are verified by using the J_0 calibration in the previous two annealing sequences. Unless the previous two annealing sequences, A1 and A2, are used, the inert ambience alone is used in this annealing sequence to understand the effect of oxygen ambience on defect formation. Because there are no other factors besides implanted damages that increase the defect growth rate, the formation of DL during annealing is reduced, as expected [see Fig. 3(c)]. The J_0 calculation also shows that SRH recombination is lower than that of A1 and A2; however, SRH is the dominant mechanism in this annealing sequence, as given in Fig. 4(a). Furthermore, removing oxygen ambience during this entire

annealing sequence improves dopant activation [as shown in Fig. 4(b)] by preventing boron segregation from silicon to oxide, which is reflected in Auger recombination as well as in surface SRH. The larger boron cluster concentration is observed than in the other two annealing sequences, A1 and A2, due to the absence of boron segregation in the implanted region, as shown in Fig. 4(c).

V. ACCOUNTING PROCESS-INDUCED DEFECTS IN DEVICE SIMULATION

As evident from Sec. V B 1, different annealing sequences cause different defect growth kinetics. However, techniques are needed to account for the defects from process to device simulation. Many previous works exist to relate these defects to J_0 ; however, understanding the effect of these defects on terminal characteristics is difficult due to a lack of models for specific process-induced defects in device simulation. Because the electrical properties of process-induced defects are not clearly understood, we have approached this problem in two different ways: (i) the SRH lifetime method (as discussed in Sec. IV) and (ii) the effective trap-density method. The SRH lifetime method is an indirect way to represent the defect, which is more about modeling the effect than the cause. On the other hand, the effective trap-density method is expected to provide more insights about the role of defects during device operation.

A. The SRH lifetime method

The surviving defects in these three annealing sequences contribute to SRH recombination. If the defects are more numerous, SRH recombination will dominate J_0 more than other recombination mechanisms. As previously stated, the calibrated boron profiles are used in the emitter region of the test structure to calibrate our simulation J_0 with the experimental J_0 using SRH lifetime. The SRH lifetime obtained from J_0 calibration is used as the emitter lifetime in the solar cell, where the emitter region will be formed using boron implantation. This SRH lifetime method is a way to study the effect of defects on the terminal characteristics of the solar cell without worrying about what caused them.

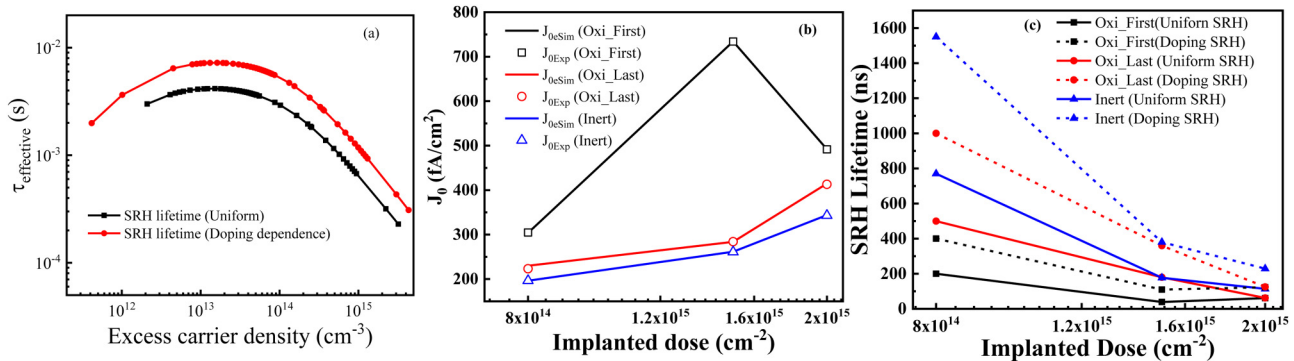


FIG. 5. Simulated quasi-steady-state photoconductance (QSSPC) results show the influence of doping on an SRH lifetime compared with a uniform SRH lifetime. (b) Simulated J_0 (solid line) matched with experimental J_0 (symbols) for all three annealing ambiances using SRH lifetime optimization. (c) Optimized SRH lifetime, which will be used as the emitter lifetime to study the influence of defects on terminal characteristics.

The constant SRH recombination model is used only to validate our J_0 extraction method (see Fig. 2), but Sentaurus TCAD offers a sophisticated model to account for dopant dependent of SRH recombination.^{48,49} In heavily doped regions, such as the emitter, doping concentration changes many orders of magnitude in a shorter distance, and the dopant solubility limit in silicon causes SRH recombination, which has an impact on the total recombination. Hence, accounting for the doping dependence of SRH recombination improves the reliability of the simulation more than accounting for a uniform SRH lifetime throughout the doped region. The difference in the SRH lifetime between the two models is shown in Fig. 5(a). For further calculations, a doping dependent SRH lifetime is used throughout the simulation. The calibrated J_0 using a doping dependent SRH lifetime for all three annealing sequences and three implanted doses is given in Fig. 5(b). Figure 5(c) shows the respective lifetimes, which will be used to calculate the solar cell terminal characteristics.

B. Effective trap-density method

Defects in implanted samples are unavoidable due to the abundance of silicon self-interstitials, even at non-amorphous implanted doses. Dislocation loops and boron clusters are two well-known defects that arise as a result of silicon interstitial supersaturation in boron implanted samples (see Fig. 3) and are widely thought to be the causes of electrical activity that impacts the terminal properties of solar cells. Sentaurus TCAD allows us to account for the defect distribution as trap density, which aids in studying the influence of defects on terminal characteristics. However, the fact that different research groups came up with different hypotheses about the role of implanted defects made it hard to figure out what each defect meant for the way the terminal characteristics of solar cells changed.

Despite the fact that numerous studies have revealed defects formed during thermal annealing followed by boron implantation, some of them associate J_0 with implantation defects. Florakis *et al.* compared their simulated implantation defects, such as interstitial concentration associated with dislocation loops and 311 defects, to

analytical J_0 ,²⁰ but the analytical J_0 is formulated for a defect-free Gaussian boron profile.⁵⁰ Pawlak *et al.*,¹⁷ and Raghuvanshi *et al.*,²³ reported that the boron cluster formed during annealing contributes to J_0 . According to Mok *et al.*,²² both the dislocation loop and the boron clusters are the reasons for recombination. Wolf reported that recombination is only caused by the dislocation loop and not by the boron clusters.⁵¹ He does this by comparing the dislocation density and the dislocation line density with their analytical J_0 and experimental J_0 . These different hypotheses make it hard for us to figure out which defects to use for calibrating our simulation J_0 with experimental J_0 and then study their effect on the terminal properties of solar cells.

1. DL as trap density

Our process simulation predicts that the DL concentration reduces from the oxidation-first annealing sequence to the inert annealing sequence (A1-A3), which is similar to the SRH recombination trend in total J_0 [see Fig. 4(a) in Sec. IV]. Hence, we chose the DL density from process simulation as the trap density in device simulation to calibrate J_0 instead of the boron cluster (refer to Sec. IV), which showed an inverse trend when comparing the SRH trend. Regarding the electrical properties of dislocation loops, the recombination associated with dislocation loops occurs via the deep energy levels in silicon.^{29,52,53} The theory explains that the concentration of deep energy levels of DL in silicon is related to the accumulation of metal impurity concentration.^{19,29,52,54} We have calibrated with the number of attached deep-level recombination centers (with the constant DL size using a constant capture cross section of 10^{-15} cm^2).⁵⁵

Previously, Wolf reported the analytical relation between the DL density [calculated using Eq. (1) (Ref. 51)] and J_0 . As stated by Wolf, a minimal DL density of around 10^7 cm^{-2} is needed to achieve SRH recombination dominant J_0 .⁵¹ The results in Fig. 6 do not reflect the latter statement. Despite the predicted lower DL density ($< 10^7 \text{ cm}^{-2}$) for the inert ambient, J_0 in Fig. 4(a) shows SRH dominant. This contradiction might be attributed to the analytical equation employed to obtain the J_0 estimate. The analytical

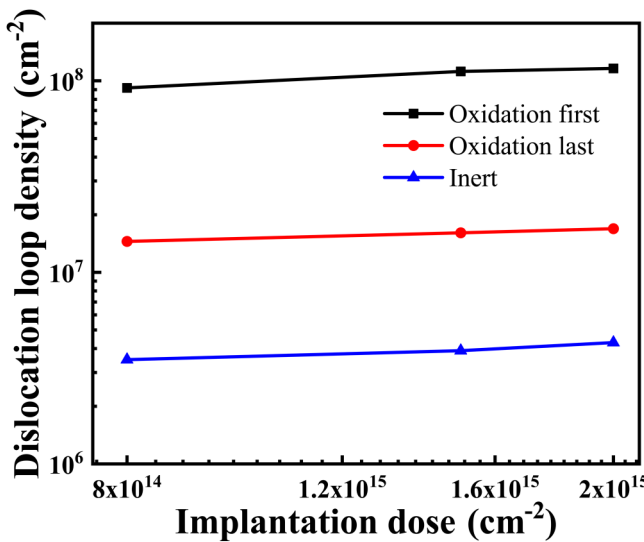


FIG. 6. SP DL density calculated using Eq. (1) for different implanted doses at different annealing ambiances.

J_0 is approximated by the square root dependence of the DL line density (ρ_L) [Eq. (2)], which is true for polysilicon (originally derived for polycrystalline silicon solar cells⁵⁶) but not necessarily for crystalline silicon. In polysilicon, the multiple crystallographic orientations are separated by grain boundaries. DL in the space charge region alone causes recombination in general;^{19,21,57,58} therefore, DL in the grain boundary of the polysilicon causes recombination. The relationship between analytical J_0 and DL may be very close to polysilicon. However, in crystalline silicon (for our case), due to high crystallinity, lower DL density compared to Eq. (2) could cause the SRH dominance (as shown in Fig. 6),

$$\text{DL density } (N) = \int D_{\text{Loop}}(x) dx, \quad (1)$$

$$J_0 \propto \sqrt{\rho_L}. \quad (2)$$

In this work, instead of using trap energies at a very deep level, we have used an acceptor energy level of 0.38 eV below the conduction band of the silicon to account for the DL effect. It is relevant in this study because it is calculated for a boron implanted sample annealed at around 1050 °C¹⁹ (see Table IV). The capture cross section (σ_c) of this acceptor trap is $1.24 \times 10^{-16} \text{ cm}^2$.¹⁹ The DL spatial-profile from the process simulation is given as the input to device simulation, as a trap distribution, to calculate J_0 as shown in Fig. 7(a). The resultant J_0 is significantly less than the experimental J_0 , indicating that the DL densities predicted from SP are not sufficient to cause the enhanced recombination observed experimentally [see Fig. 7(b)].

VI. FITTING THE DIFFERENT EXPERIMENTAL REVERSE J-V DATA TO CAPTURE PROCESS-INDUCED DEFECTS

In Sec. V B 1, we showed that the simulated DL profile does not explain the recombination mechanism that kills the photo-carrier lifetime. In this section, we will show that the experimentally measured DL profile¹⁹ does not explain the recombination mechanism as well.

We tried calibrating a different set of experimental reverse J-V data from Nyamhere *et al.*,¹⁹ which was used to explain the role of DL in reverse current. They carried out a deliberate experiment to keep the DL in the space charge region (SCR) of the n-type silicon diode to study the electronic properties of DL. The boron is implanted in pre-amorphous silicon, and the sample is annealed at two different annealing conditions, which are 1000 °C for 15 s annealing and 1100 °C for 300 s annealing time. The reference diode (non-amorphizing implant) J-V is used for comparison to study the effect of DL on reverse current. They have calculated the trap energy level (an acceptor trap of 0.38 eV below the conduction band) and capture cross section ($1.24 \times 10^{-16} \text{ cm}^2$) of DL using the DLTS experiment. The DL spatial distribution was measured for both annealing conditions. We used measured DL spatial and energetic distributions for the calibration of reverse current density for both annealing conditions of boron implanted samples.

TABLE IV. Reported parameters of implanted defects for different annealing conditions.

S. no.	Defect	Defect type	Wafer polarity	Type of study	Energy level (eV)	Capture cross section (cm²)	Annealing temperature and time	Reference
1	Dislocation loop	Acceptor	n-type	Experiment	Ec - 0.38	1.24×10^{-16}	1000 °C and 1100 °C 15 and 300 s	19
2					Ec - 0.40	...	900 °C	61
3					Ec - 0.40	...	600–900 °C 30 min	62
4		Donor	p-type	Experiment	Ev + 0.25	...	1000 °C and 1100 °C 15 and 300 s	19
5					Ev + 0.47	...	900 °C	61
6					Ev + 0.54	...	600 °C–900 °C 30 min	62
7	BI ₂	Acceptor	-	Density functional	Ev + 0.53	63
8	B ₂ I ₂			functional	Ev + 0.47			
9	B ₂ I ₃			theory	Ev + 0.40			
10	B ₃ I ₃				Ev + 0.22			
11	311	Acceptor	n-type	Experiment	Ec - 0.54	2.3×10^{-15}	500–800 °C 10 min	64

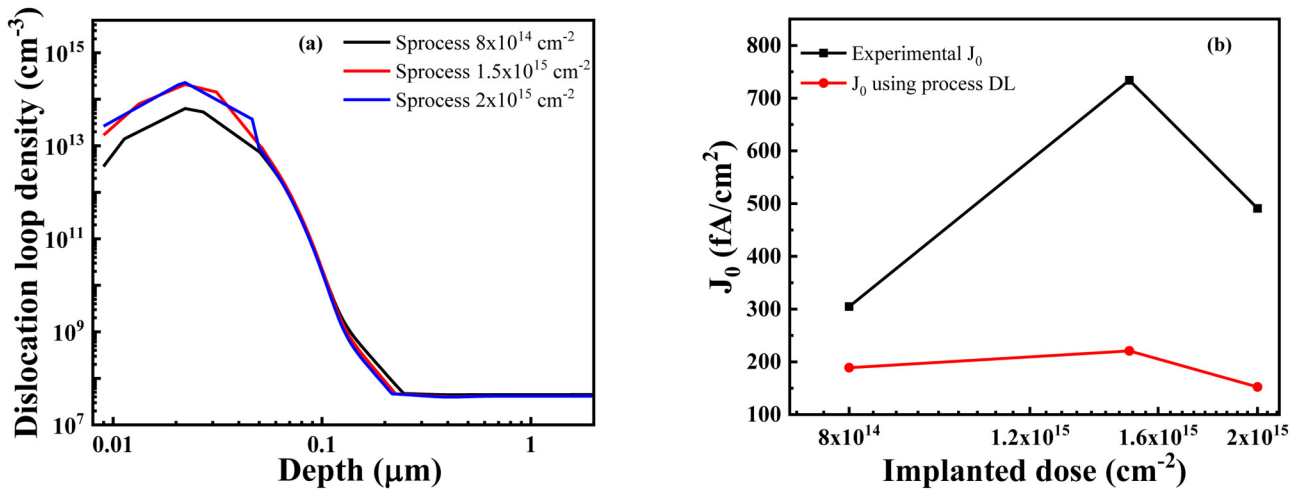


FIG. 7. (a) The SP DL profile is used as the trap density in the device simulation to calibrate J_0 . (b) J_0 was calculated using the SP DL profile for the oxidation-first annealing sequence, which has a larger deviation.

We begin our calibration with the reference diode, which will assist us in determining some fundamental physical parameters before calibrating the amorphizing implant samples. We have fitted the reference J-V as shown in Fig. 8(a), and the parameters are given in Table III. Because the reference sample is deemed defect-free, the bulk and emitter lifetimes are kept at 1 ms. However, to explain reference J-V curve, a uniform donor trap density of $5.5 \times 10^{17} \text{ cm}^{-3}$ is required at the lower half of the silicon bandgap, closer to the valence band of silicon in the boron-doped region (emitter), as shown in the schematic Fig. 8(b). This is found using a heuristic approach in our device simulation. Since the reference

diode reverse J-V is from a non-amorphizing sample, fewer DLs or boron clusters may contribute to this donor defect density in the heavily doped region. However, higher donor trap densities are required to calibrate the reverse J-V curve. Further work is needed to determine how this larger trap density was formed.

The boron implanted sample was annealed at a temperature of 1000 °C for 15 s to study the effect of DL on diode terminal characteristics. The DL concentration is deliberately kept in the SCR, which has a higher impact on reverse current than DL in a quasi-neutral region. To calibrate the J-V in a reverse bias, the DL measured spatial and energetic distribution is given as an input to the

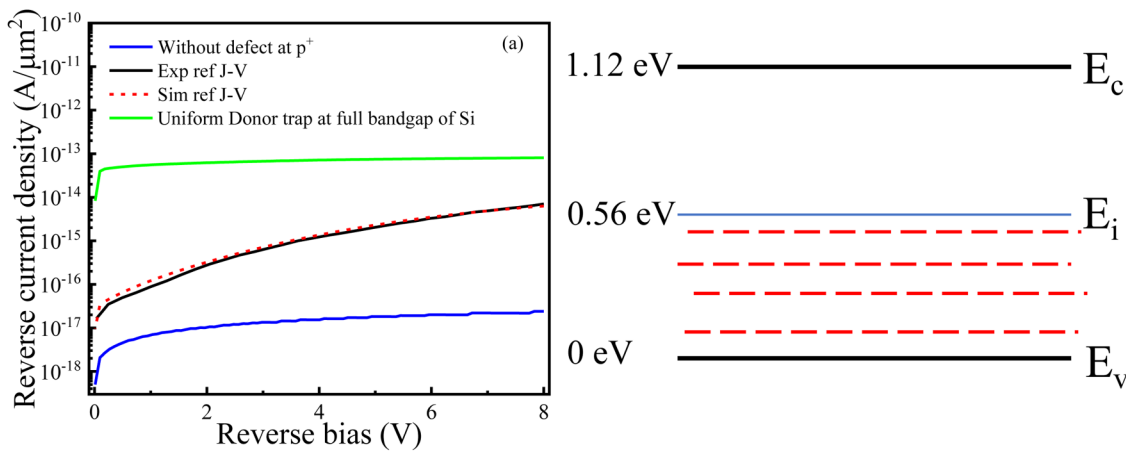


FIG. 8. (a) Calibrated reference J-V curve. The blue line represents J-V without any traps, the red dotted line represents calibration using donor trap density, and the green line represents donor trap density throughout the bandgap. (b) A schematic of the energetic distribution of donor traps (uniformly distributed in a boron-diffused region) used to calibrate the reported J-V curve.

TABLE III. Physical parameters used to calibrate the diodes' reverse J-V curves.

S. no.	Physical properties	Reference sample	1000 °C_15 s	1100 °C_300 s
1	p ⁺ region lifetime	1 ms	1 ms	1 ms
2	Bulk lifetime	1 ms	1 ms	1 ms
3	Trap density at the p ⁺ region	$5.5 \times 10^{17} \text{ cm}^{-3}$	$5.5 \times 10^{17} \text{ cm}^{-3}$	$2.7 \times 10^{20} \text{ cm}^{-3}$
4	Trap energetic distribution at the p ⁺ region	Uniform (donor trap)	Uniform (donor trap)	Uniform (both donor and acceptor)
5	Capture cross section at p ⁺ DL	$2 \times 10^{-16} \text{ cm}^2$	$2 \times 10^{-16} \text{ cm}^2$	$2 \times 10^{-16} \text{ cm}^2$
6	DL trap level and capture cross section	Nil	Given as profile	Given as profile
7	Bulk trap density	...	$E_c - 0.38 \text{ eV}$ and $1.24 \times 10^{-16} \text{ cm}^2$	$E_c - 0.38 \text{ eV}$ and $1.24 \times 10^{-16} \text{ cm}^2$
8	Bulk trap energetic distribution (assumed spatially uniform)	...	$5 \times 10^{18} \text{ cm}^{-3}$	$3 \times 10^{16} \text{ cm}^{-3}$
10	Bulk trap capture cross section	...	$1 \times 10^{-15} \text{ cm}^2$	$1 \times 10^{-15} \text{ cm}^2$

device simulation, as shown in Fig. 9(a). As expected from the calibration, the DL has a negative impact on reverse current density when compared to the reference J-V. However, the whole story is not around DL, as suggested in the reference to this annealing condition, which is given in Fig. 9(b). The parameters used to calibrate [see Fig. 9(c)] J-V in this annealing condition are listed in Table III. The reverse current at this annealing condition is fully controlled by the bulk defect, which is around $5 \times 10^{18} \text{ cm}^{-3}$ [a uniform donor trap near the valence band of the bulk as shown in Fig. 8(b)]. This counter-intuitive result is possible because of the formation of small silicon interstitial defects that are deeper in the bulk and harder to detect.^{59,60} Even at short annealing times, these interstitial defects can diffuse faster into the bulk, effectively reducing the bulk lifetime.⁵⁹ Since we do not know the electronic properties of small silicon interstitial defects, we used a uniform trap energy level. The capture cross section is assumed to be 10^{-15} cm^2 .

The reverse current is dominated by small interstitial defects rather than DL at the annealing condition of 1000 °C for 15 s,

which contradicts the reference. At the same time, we cannot deny that DL has some negative effects on reverse current by increasing the chances of SRH recombination. At an annealing temperature of 1100 °C and an annealing duration of 300 s, reverse current exhibits some unusual trends over voltages. The current density at a reverse bias increases linearly with increasing voltages. To calibrate J-V at this annealing condition, separate understanding is needed for the lower voltage regime (0–1 V) and the higher voltage regime (1–8 V). In the lower voltage regime, reducing bulk defects makes it easy to calibrate the reverse current density, as shown in Fig. 10(a). The bulk defects (small interstitial defects) that are prominent at low annealing conditions (1000 °C) start to disappear at this higher annealing temperature. In the higher voltage regime, current density increases exponentially with voltage (as it looks linear in the semi-log plot, we call it the “linear” region), which cannot be explained using uncompensated boron diffusion. However, the excess boron diffusion [see Fig. 10(b)], though it undoubtedly has some negative effects, does not explain the voltage dependence at higher voltages as given in Fig. 10(a).

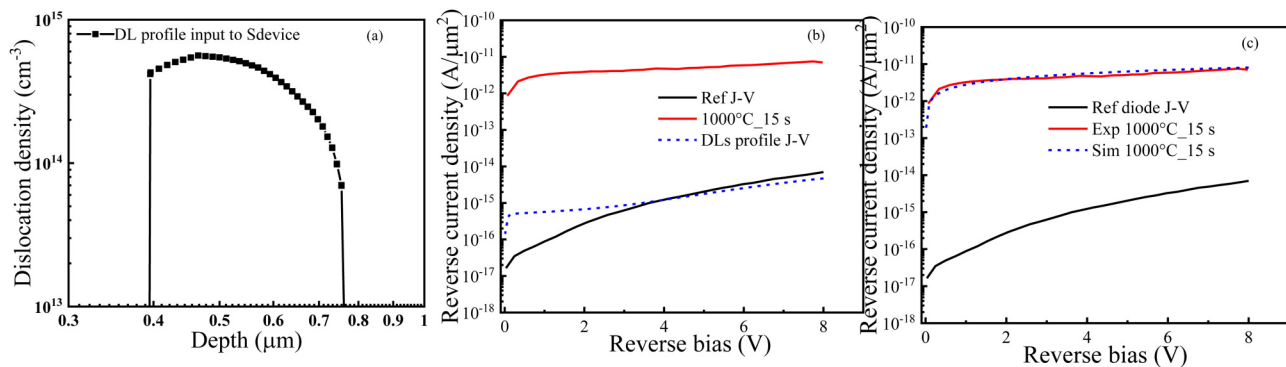


FIG. 9. (a) Reported experimental DL profile, which is given as an input to the Sentaurus device at SCR. (b) DL contribution (blue line) to the reverse current density, but some phenomena are missing to calibrate the J-V with experiments (red line). (c) Calibrated J-V using bulk trap density (blue line), which is contributed by small interstitial defects.

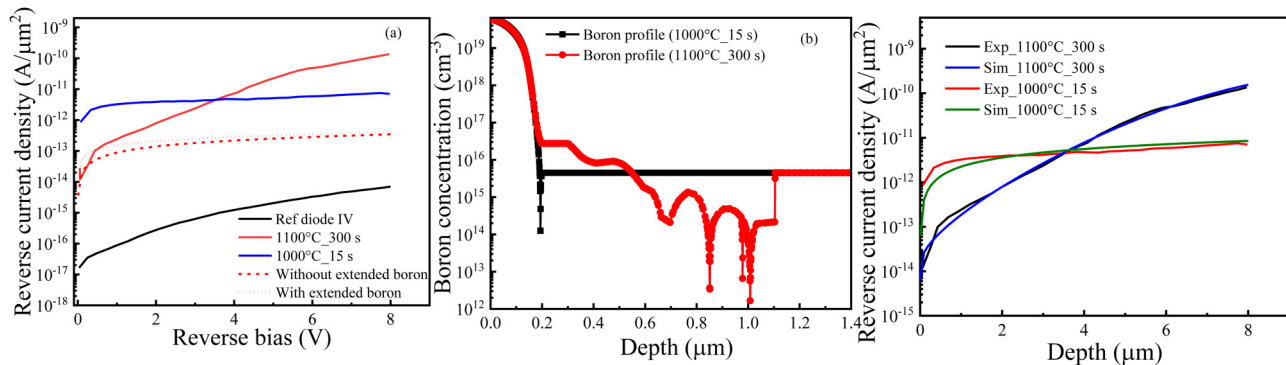


FIG. 10. (a) Simulated J-V curves (dashed and dotted lines) calibrated at a lower voltage regime (<1 V) using bulk trap density and experimental J-V curves (solid lines). (b) Reported experimental boron profiles at different annealing conditions. (c) Calibrated J-V curves using an SRH lifetime.

In the previous literature,¹⁹ a coupled defect level (CDL) is used to explain the linear increase in the current at higher reverse voltages (>4 V). We explain with a different mechanism as discussed below. The reverse J-V at higher annealing conditions for 1100 °C at 300 s is calibrated using tabulated parameters as shown in Table III. The calibrated reverse J-V is shown in Fig. 11. Even though similar fitting was done by Nyamhere *et al.* using coupled-defect levels, we show here that fitting can be done using independent defects as well. This further validates our previous finding (see Sec. V B) that the dislocation loop alone could not explain the process-induced recombination mechanisms.

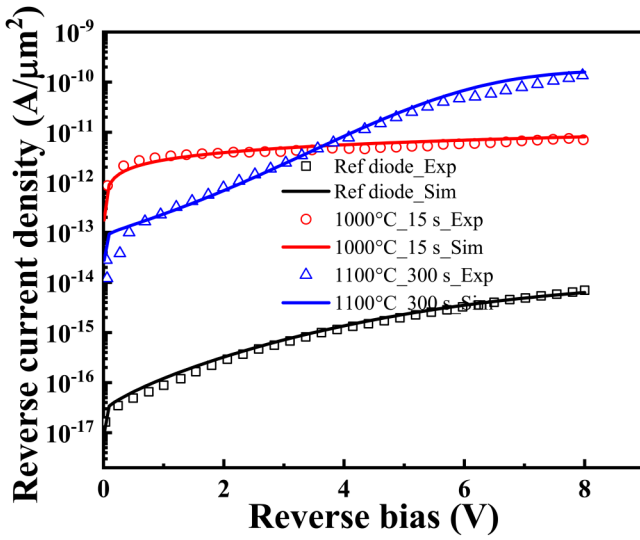


FIG. 11. Fully calibrated J-V curves of boron implanted and diffused (reference) p^+ n diodes. The defects formed during implantation and annealing cause an increase in reverse current by facilitating SRH recombination.

A. Independent trap densities to fit the reverse-biased J-V curves

To explain the higher voltage regime of J-V, trap density is considered to be around $2 \times 10^{20} \text{ cm}^{-3}$ in the area where boron was implanted (the emitter). The experimentally reported DL density is low at high annealing conditions (1100 °C and 300 s), which is fed as an input for device-level simulation. Despite that, we needed a higher trap density in the emitter region to explain the reverse J-V curve. The cause of the higher trap density in the implanted region is currently unknown. However, DL and small interstitials (bulk defects) formed during annealing do not contribute to it. Our simulation predicts that (i) defects formed in the emitter will contribute to the current density at higher reverse voltages and (ii) defects formed in bulk will contribute to the current density at lower reverse voltages.

When we introduce the donor trap (as from the experience of calibrating the J-V of a reference sample, see Table III) into the emitter region (p-side), the fitting shows the concentration to be around $2 \times 10^{20} \text{ cm}^{-3}$. The ideal reverse bias is discussed in Appendix B. The newly introduced donor trap density on the p-side captures the majority charge carrier, i.e., holes. To bring them back to equilibrium, the law of mass action enhances the minority charge-carrier concentration at equilibrium, as shown in Fig. 12(a). Unfortunately, due to the early saturation of current density at reverse voltages of around 4 V, we are unable to fully explain the J-V using donor trap density alone [see Fig. 12(b)]. However, the linearity of current density up to 4 V is governed by increased minority carrier (electron) density at equilibrium due to the introduced majority carrier (donor) trap density in the p-doped region. Above 4 V, the minority carrier concentration starts to saturate, and the current gets saturated, in contrast to the reported experimental data as shown in Fig. 12(c). To calibrate the current at voltages above 4 V, we introduced the minority carrier (acceptor) trap around the same number as the majority carrier (donor) trap in the p-doped region, which explains the J-V curve more accurately. After 4 V, the trapped minority charge carrier begins to emit from the trap and contribute to conduction, which is given in the trapped carrier plot in Fig. 12(d). After introducing the acceptor

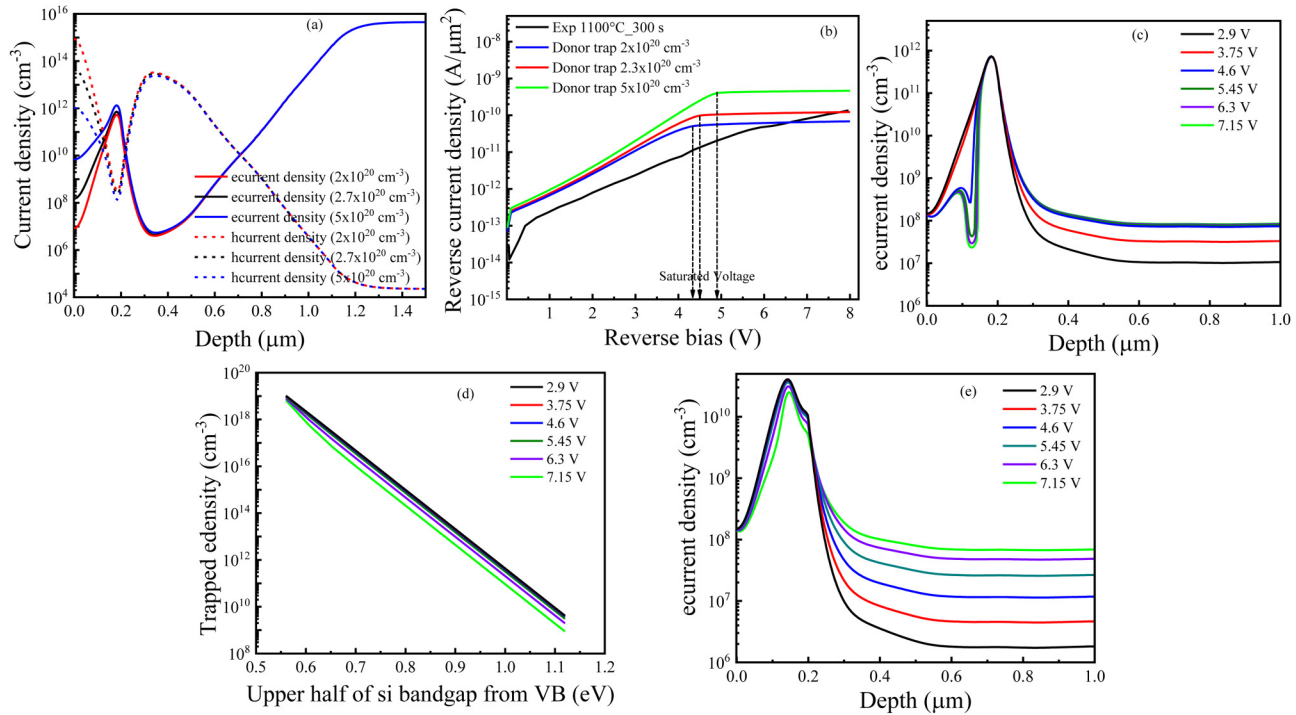


FIG. 12. (a) Current density at equilibrium; the dotted line represents hole current density at various donor trap densities; the solid line, similarly, represents electron current density. (b) Reverse J–V at different donor trap densities, which saturate earlier around 4 V. (c) Electron current density at different voltages, which reduces at higher voltages; hence, J–V saturates. (d) Trapped electron density at different voltages after introducing acceptor trap density. (e) The electron emission from the trap at a higher voltage ensures the availability of electrons, which linearly increases the current.

state, the reduced electron concentration at a higher voltage is compensated by the re-supply of captured electrons by the acceptor states, as shown in Fig. 12(e). Hence, the J–V is linearly (on a semi-log scale) increasing after 4 V, thereby allowing us to calibrate the J–V. Hence, both trap densities are needed to explain the J–V curve at higher annealing conditions.

B. Reason for the enhanced recombination

Our simulations in comparison with the experimental data confirm that DL alone cannot explain the enhanced recombination (or excess reverse-biased current). Boron cluster could not be the possible defect mechanism as well for the following reason: simulation estimated boron cluster density is in an opposite trend with the experimentally measured J_0 ,²⁰ and also, simulated J_0 mismatches with the reported one (results not shown here). Therefore, we conclude that either there must be coupled defects between DL and other defects (as shown in Nyamhere's work) or independent defects other than DL could be the possible recombination-inducing pathways (as shown in this work in Fig. 11).

To further study the effect of process-induced defects on the solar cells' performance, we used the SRH lifetime and effective trap density (independent defect contribution). As we are not able to reverse engineer the origin of the defects with the available data

(see Table IV), we have used the single trap energy to effectively capture the effect on the solar cell performance. We optimized the independent defect concentration (D_c) to fit the reported J_0 with the trap energy of 0.56 eV above the valence band and an assumed capture cross section of 10^{-15} cm². The optimized D_c is tabulated in Table V, which is used in the device-level simulation in Sec. VII.

TABLE V. Fitted effective trap density with the trap energy of 0.56 eV above the valence band and the assumed capture cross section of 10^{-15} cm⁻².

S. no.	Annealing sequence	Dose (cm ⁻²)	Optimized D_c (cm ⁻³)
1	Oxidation first	8×10^{14}	1.24×10^{14}
		1.5×10^{15}	4.55×10^{14}
		2×10^{15}	4.02×10^{14}
2	Oxidation last	8×10^{14}	4.8×10^{13}
		1.5×10^{15}	1.35×10^{14}
		2×10^{15}	3.92×10^{14}
3	Inert	8×10^{14}	4×10^{13}
		1.5×10^{15}	1.6×10^{14}
		2×10^{15}	2.6×10^{14}

VII. TERMINAL CHARACTERISTICS OF PERT SOLAR CELLS

A. n-PERT solar cell J-V calibration

Before studying the deleterious effect of process-induced defects on terminal characteristics, simulation solar cells J-V are calibrated with experimental J-V. A bifacial n-PERT solar cell is calibrated, and the schematic is shown in Fig. 13(a). The boron profiles of an emitter and a selective emitter and the back junction polysilicon passivating contact parameters are adapted from Ref. 65. Even though the pinhole in the passivation oxide layer and band to band tunneling contribute to charge-carrier transport,^{66–68} we assumed only direct band to band tunneling (not accounting for pin-hole transport) as a transport mechanism in the back junction of

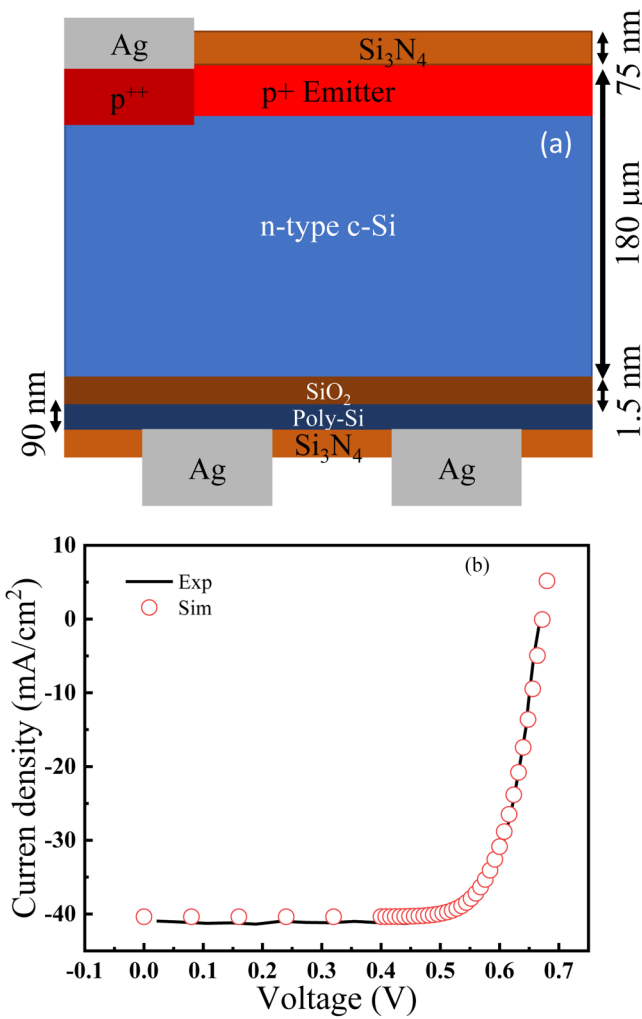


FIG. 13. (a) Schematic of an n-type bifacial PERT solar cell. (b) The calibrated simulation and the reported experimental J-V curve of a bifacial n-type PERT solar cell.

a bifacial cell for simplicity's sake. The calibrated J-V is shown in Fig. 13(b). The optical generation rate is computed using the AFORS-HET simulation tool with a random pyramid surface design, and no free carrier absorption is considered.

B. Effect of boron profile on the ideal solar cell

The optimized SRH lifetime during J_0 calibration is used as the emitter lifetime of a bifacial cell to investigate the effect of a process-induced defect, and the remaining parameters are the same as used during J-V calibration. The optimized boron profile from process simulation is used in the emitter region of the PERT cell. To illustrate the influence of process defects in a bifacial solar cell, assume an ideal cell with a defect-free emitter and an SRH lifetime of 1 ms. The efficiency of the ideal cell for all three annealing sequences is shown in Fig. 14(a). The efficiency of the A1 annealing sequence increases with the implanted dosage, but the A3 annealing sequence has a reverse tendency. The efficiency decreases as the implanted dose increases.

Because of boron segregation into oxide, dopant activation is lower in the A1 annealing sequence than in the other two annealing sequences, as seen in Fig. 4(c). Therefore, the series resistance reduces (conductivity increases) with increasing boron dose in the emitter, which is evident by looking at the fill factor (FF) over the implanted dose in Fig. 14(b). The slope of the FF shows how the A1 annealing sequence is restricted due to series resistance; hence, efficiency increases with dose. Even so, as shown in Figs. 15(a) and 15(b), V_{oc} and J_{sc} decrease with the dose due to increased Auger recombination (the dominant recombination mechanism under short-circuit conditions). Efficiency rises due to FF's dominance.

In the case of A3 annealing, efficiency decreases with an increasing implanted dose [see Fig. 14(a)]. As we know, the dopant activation is larger in the A3 annealing sequence than the other two annealing sequences. As a result, Auger recombination takes over under short-circuit conditions as given in Fig. 15(b), affecting V_{oc} and J_{sc} . Even though there is a slight increase in FF due to reducing the series resistance with the implanted dose [see Fig. 14(b)], J_{sc} and V_{oc} influence the efficiency more than the FF increase. The A2 annealing sequence clearly shows the trade-off between J_{sc} , V_{oc} , and FF over the boron implanted dose. The efficiency rises significantly when the dose is increased to $1.5 \times 10^{15} \text{ cm}^{-2}$, and then it begins to decrease when the implanted dose is increased further.

C. Effect of annealing ambience on the PERT solar cell using an SRH lifetime method

The terminal characteristics of bifacial cells with SRH lifetime as emitter lifetime show the deviation from ideal cell efficiency, which confirms the negative effect of process-induced defects on terminal characteristics as shown in Fig. 16(a). The A3 annealing sequence performs better than all other annealing processes, especially when compared to the A1 annealing process, which is better by 0.19% at a dose of $8 \times 10^{14} \text{ cm}^{-2}$. This improvement is due to the reduced process defects in the A3 process, which shows the significance of the optimal process conditions. Even though the SiO_x surface passivation was lost during inert atmosphere annealing, it can be made up for by adding more passivation stacks, such as

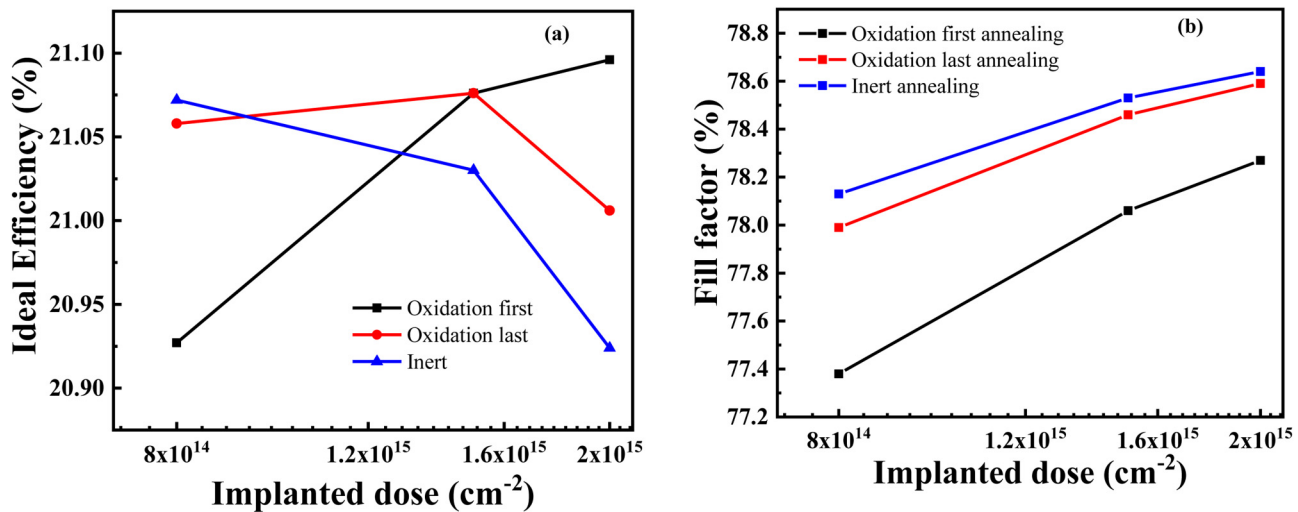


FIG. 14. (a) Power conversion efficiency of defect-free (assumed high SRH lifetime of 1 ms) n-PERT bifacial solar cells at different doses of implanted boron for all three annealing sequences. (b) FF variations over the implanted dose for different annealing sequences.

$\text{AlO}_x/\text{SiN}_x$. The deviation is measured, and as anticipated from the SRH lifetime, the A1 annealing sequence has a bigger departure from ideal efficiency than the other two, with the greatest of 6% in the A1 annealing sequence shown in Fig. 16(b). The terminal characteristics of the bifacial PERT cell are given in Fig. 17 for all three annealing sequences at an implanted dose of $8 \times 10^{14} \text{ cm}^{-2}$.

The reduced defects in the A2 annealing sequence improve V_{oc} over oxidation-first annealing, and the defects are further reduced in the A3 annealing. Moreover, V_{oc} faces a slight reduction in the A3

annealing sequence as given in Fig. 17(a), which could be Auger dominant in total recombination over defect-induced SRH recombination at short-circuit conditions. Reduced J_{sc} owing to Auger recombination, will cause increases from A1 annealing to A3 caused by enhanced dopant activation due to less boron segregation. However, the efficiency follows the FF trend, as shown in Fig. 17(b). The FF increases when annealing sequences are changed from A1 to A2 and A3 annealing due to enhanced conductivity, as shown in Fig. 17(c), which enhances the selectivity of holes in boron-doped emitters.

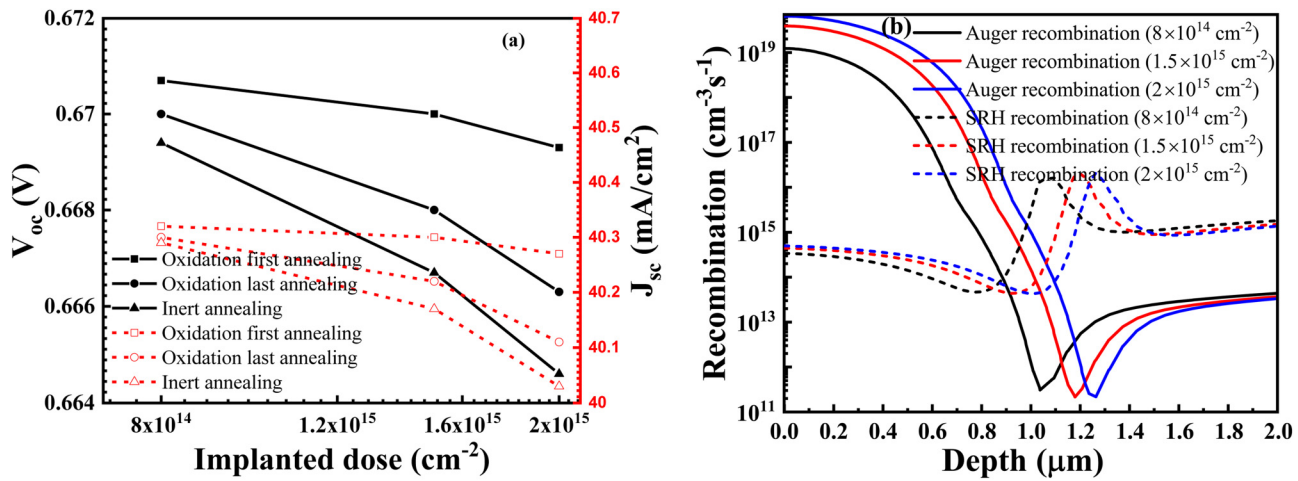


FIG. 15. (a) V_{oc} and J_{sc} of an ideal cell. The black solid line represents V_{oc} , and the red dashed line represents J_{sc} . (b) Auger and SRH recombination contributions for inert annealing at a maximum power point voltage (simulated at 0.55 V). Auger recombination is represented by a solid line, while SRH recombination is represented by a dashed line.

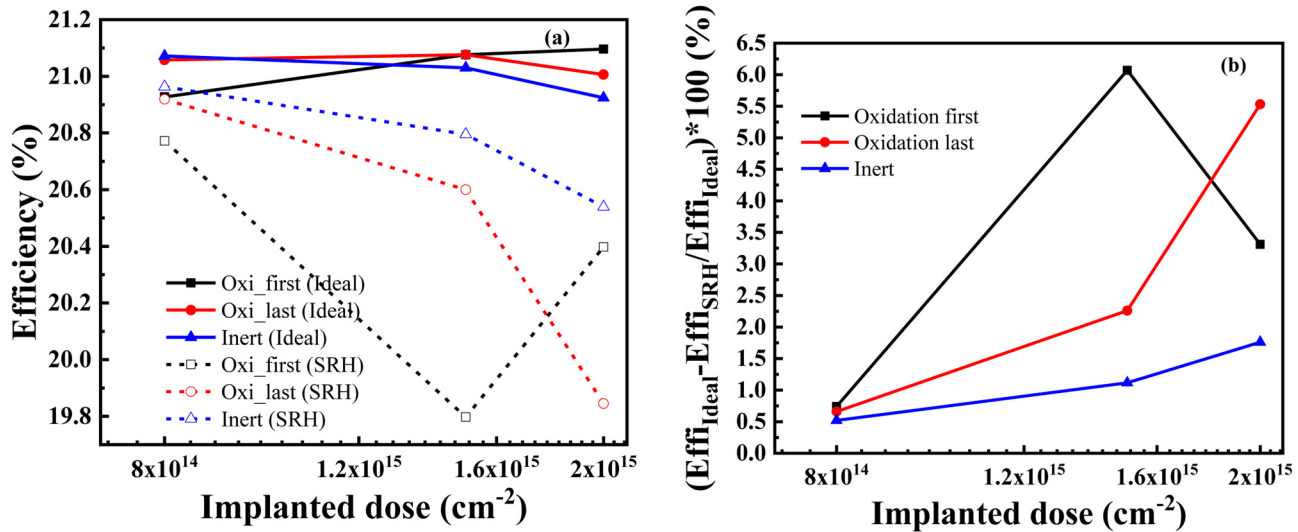


FIG. 16. (a) Defect-accounted efficiency (using SRH lifetime, dashed lines) vs defect-free efficiency (solid lines) for all annealing sequences. (b) Relative change in efficiency for all three annealing sequences—indicating the strong role of process-induced defects in an oxidation-first annealing sequence.

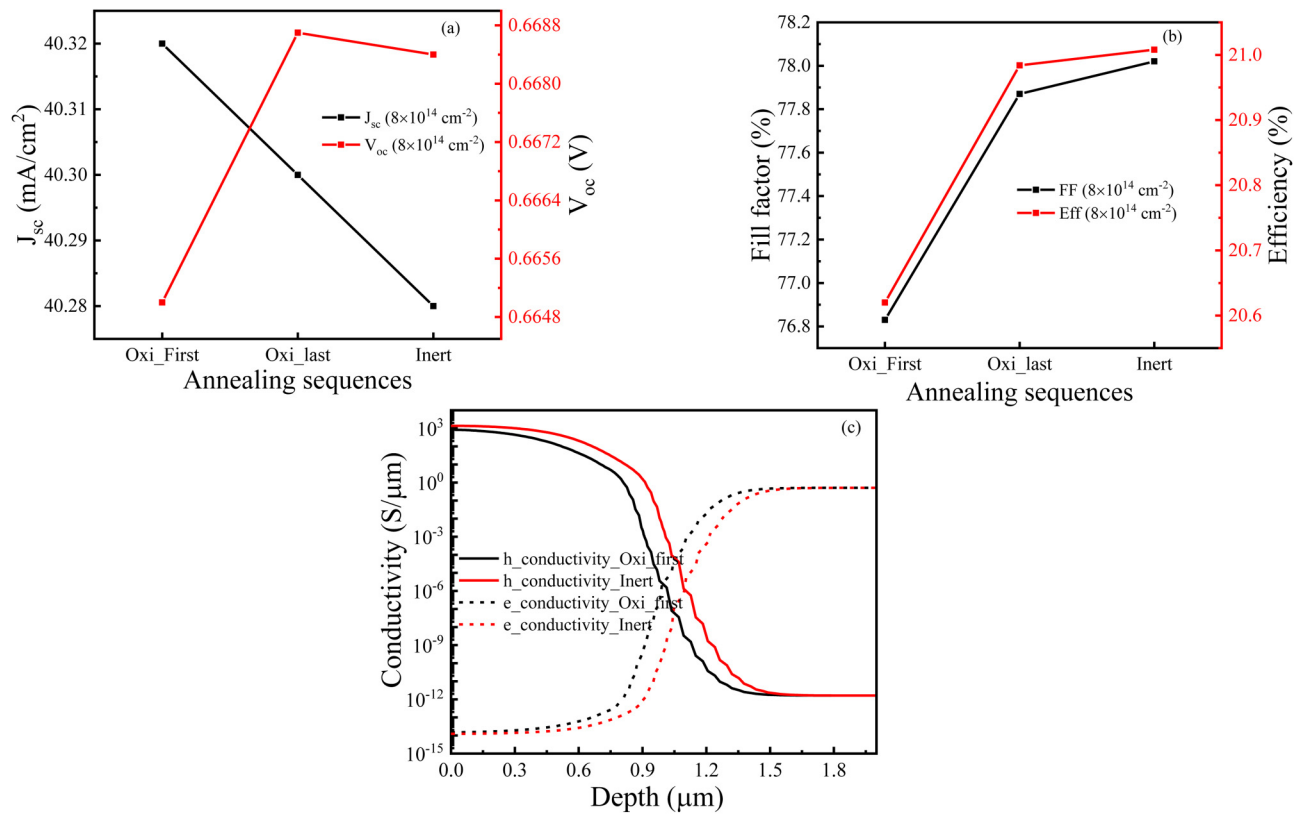


FIG. 17. (a) V_{oc} and J_{sc} change with annealing sequences at an implanted dose of $8 \times 10^{14} \text{ cm}^{-2}$. (b) FF and efficiency change with annealing sequences at an implanted dose of $8 \times 10^{14} \text{ cm}^{-2}$. (c) The simulated conductivity profile of electrons and holes in a boron implanted emitter for oxidation-first (Oxi-first) and inert annealing sequences.

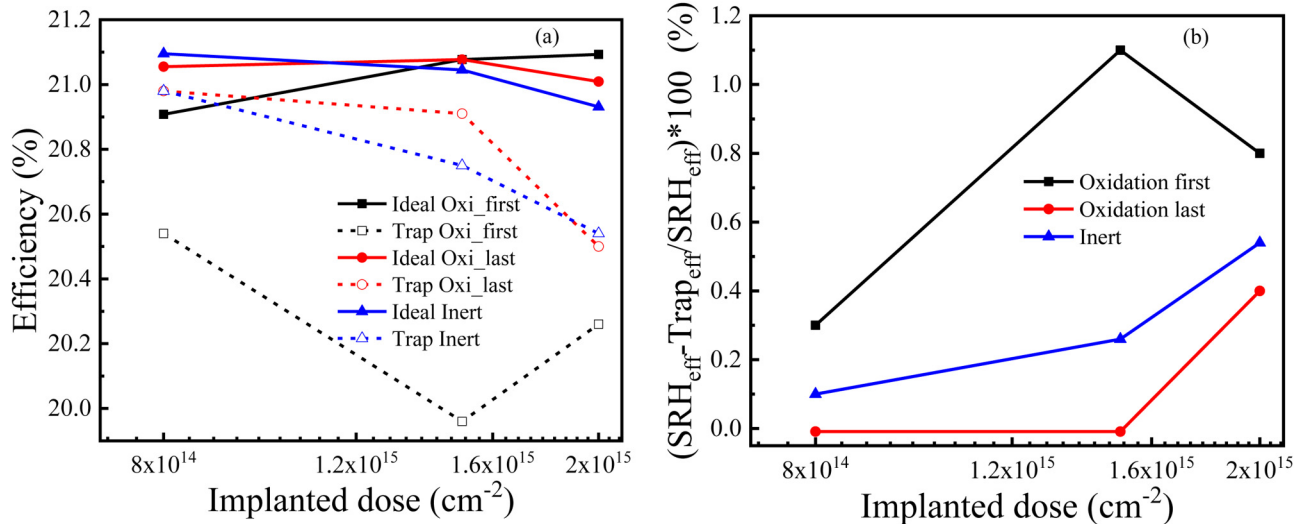


FIG. 18. (a) Defect-accounted efficiency (using a trap-density method, dashed lines) vs defect-free efficiency (solid lines) for all annealing sequences. (b) The relative change in the efficiency between the two methods (SRH lifetime and the effective trap-density method) for all three annealing sequences—which shows ignorable variations.

D. Effect of annealing ambience on a PERT solar cell using effective trap density

The optimized trap density is used to facilitate SRH recombination in the emitter region of the bifacial solar cell. The calculated efficiency using trap density is compared with the ideal efficiency, which is shown in Fig. 18(a). The difference between ideal and trap-density efficiency is almost similar to the SRH lifetime method. The contraction between the SRH lifetime method and the trap-density method is less, which is plotted in Fig. 18(b). Overall, the deviation between these two methods is less than 1%. Interestingly, the oxidation-last annealing sequence and the inert annealing sequence nearly match each other. For the quantitative analysis, we can follow any one of the methods to account for the impact of a defect on device simulation. However, the trap-density method along with detailed trap electrical properties may provide further insights because they could possibly explain both the phenomenon (how the defects affect the device performance) and its impact on device terminal characteristics. This might be used to reverse engineer to find the defect origin as well.

VIII. CONCLUSIONS

The defect formation kinetics for three different annealing sequences (A1, A2, and A3) has been investigated. The effect of these defects on the terminal characteristics of the n-PERT solar cell is investigated using (i) SRH lifetime and (ii) effective trap density. Because the simulated and measured DL does not explain the J_0 and experimentally measured diode reverse current, the independent defects are used as the optimizing parameter to calibrate the

experimental J_0 . The calibrated SRH lifetime and the trap density are used in the emitter and bulk regions of the n-PERT solar cell to study the impact of the defect on terminal characteristics. Both the methods effectively captured the performance loss due to process-induced defects in solar cells, which shows deterioration of almost 1% absolute power conversion efficiency. However, the effective trap-density method might give more insights about the defect's origin. The efficiency of n-PERT solar cells can be enhanced from 19.8% to 21% by carefully optimizing the process sequence, which in turn alters the process-induced defects.

ACKNOWLEDGMENTS

This work was supported in part by the Department of Science and Technology, India, through the Fund for Improvement of S&T Infrastructure Programme under Grant Nos. SR/FST/ETI-338/2013 and SR/FST/ETI-349/2013. The work of Sangaravadivel Masilamani was partially supported by the CSIR for a Senior Research Fellowship under Grant No. 143366/2K18/1 [File No. 09/1095(0045)/19-EMR-I]. The authors would like to thank the reviewers for improving the manuscript's quality considerably.

AUTHOR DECLARATIONS

Conflict of Interest

The authors have no conflicts to disclose.

Author Contributions

Sangaravadivel Masilamani: Conceptualization (equal); Data curation (equal); Funding acquisition (equal); Investigation (equal);

Validation (equal); Visualization (equal); Writing – original draft (equal); Writing – review & editing (equal). **Ramachandran Ammapet Vijayan:** Conceptualization (equal); Data curation (equal); Formal analysis (equal); Validation (equal); Visualization (equal); Writing – original draft (equal); Writing – review & editing (equal). **Muthubalan Varadharajaperumal:** Data curation (equal); Formal analysis (equal); Resources (equal); Software (equal); Supervision (equal).

DATA AVAILABILITY

The data that support the findings of this study are available within the article.

APPENDIX A: RECOMBINATION MECHANISM

The emitter (SRH, Auger, and radiative) recombination current (J_E) and the surface recombination current (J_{surf}) are calculated using the following relations:

$$J_E = q \int_0^{x_j} R_E(x) dx,$$

$$J_{surf} = q \times R_{surf},$$

where q is the elementary charge, x_j is the junction depth, and R_E/R_{surf} is the bulk/surface recombination rates. The bulk/surface recombination percentage is computed by

$$\text{Individual Contribution (\%)} = \frac{J_{rec}}{J_{tot}} \times 100,$$

where J_{tot} is the electron current density extracted at the junction depth (x_j) at 0.55 V and J_{rec} is J_E/J_{surf} at 0.55 V. The total electron flux entering the emitter (e_{tot}) under a forward bias and its corresponding recombination loss in the emitter (e_E) and at the surface (e_{surf}) are depicted in Fig. 19 (the electron flux rather than the

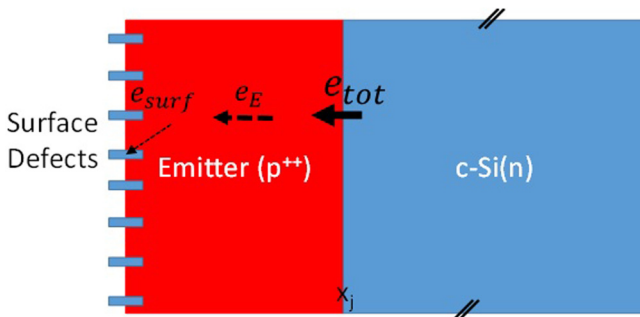


FIG. 19. Schematic to explain the J_0 splitting. The electron flux rather than the electron current direction is preferred for better clarity. In the cartoon, only a few electrons are lost in the bulk emitter recombination, which is indicated by the arrow thickness.

electron current direction is preferred for better clarity to the readers).

APPENDIX B: IDEAL REVERSE J-V

In an ideal diode (without defects), at a reverse bias, the minority charge carrier causes a small, steady flow of current. The minority charge carriers are relatively few in number in the heavily doped region due to the law of mass action ($np = n_i^2$). Hence, the reverse current is saturated even at very small reverse voltages. However, in our case, reverse current increases linearly with voltage. However, introducing trap density in the emitter region will allow us to calibrate the increasing current density. Fig. 20(a) illustrates the schematics of the PN junction diode under a reverse bias. When the electron is injected from the battery to the valence band of the p-side of the diode, equilibrium gets disturbed due to the excess electron on the p-side of the diode. To keep the balance, the hole (from the p-side) recombines with the electron. Now, holes from the diode's n-side will diffuse to the p-side, restoring full p-side equilibrium. The electron-hole pair will be generated in the SCR, which balances the hole loss in the n-side, and the excess generated electron will come out of the conduction band of the n-side. Whenever an electron-hole pair is generated at the reverse bias, an electron will come out of the diode and go to the battery (this is the reason the reverse current is called generation current). When the donor and acceptor trap densities are introduced into the

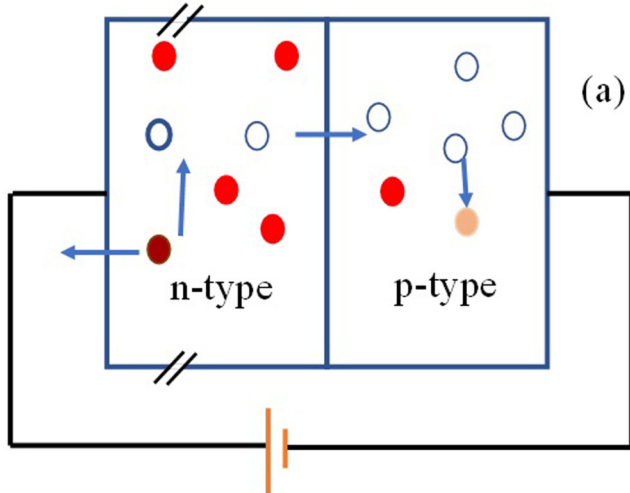


FIG. 20. (a) Diagram of an ideal diode with a reverse bias, with orange dots representing injected electrons, red dots representing equilibrium electrons, and brown dots representing generated electrons. The open dots are equilibrium holes, and the highlighted open dots are generated holes. The down arrow represents recombination, the up arrow generation, the arrow pointing from an n-type to a p-type represents hole diffusion, and the leaving arrow at the n-side represents electrons exiting the terminal.

boron implanted region, they produce a linear reverse J-V curve (see Sec. VI A).

REFERENCES

- ¹P. Würfel, *Physics of Solar Cells: From Basic Principles to Advanced Concepts* (Wiley, 2009).
- ²S. Kashyap, J. Madan, and R. Pandey, *Sustain. Energy Fuels* **6**, 3249 (2022).
- ³J. Krügener, H. J. Osten, F. Kiefer, F. Haase, and R. Peibst, in *Proceedings of the International Conference on Ion Implantation Technology* (Institute of Electrical and Electronics Engineers, Inc., 2017).
- ⁴J. Krügener, H. J. Osten, F. Kiefer, F. Haase, and R. Peibst, in *2016 21st International Conference on Ion Implantation Technology (IIT)* (IEEE, 2016), pp. 1–5.
- ⁵M. G. Kang, J. H. Lee, H. Boo, S. J. Tark, H. C. Hwang, W. J. Hwang, H. O. Kang, and D. Kim, *Curr. Appl. Phys.* **12**, 1615 (2012).
- ⁶A. Rohatgi, D. L. Meier, B. McPherson, Y.-W. Ok, A. D. Upadhyaya, J.-H. Lai, and F. Zimbardi, *Energy Procedia* **15**, 10 (2012).
- ⁷H. Hieslmair, L. Mandrell, I. Latchford, M. Chun, J. Sullivan, and B. Adibi, *Energy Procedia* **27**, 122 (2012).
- ⁸R. Low, A. Gupta, N. Bateman, D. Ramappa, P. Sullivan, W. Skinner, J. Mullin, S. Peters, and H. Weiss-Wallrath, in *2010 35th IEEE Photovoltaic Specialists Conference* (IEEE, 2010), pp. 1440–1445.
- ⁹R. Müller, C. Reichel, J. Benick, and M. Hermle, *Energy Procedia* **55**, 265 (2014).
- ¹⁰C. E. Dubé, B. Tsefrikas, D. Buzby, R. Tavares, W. Zhang, A. Gupta, R. J. Low, W. Skinner, and J. Mullin, *Energy Procedia* **8**, 706 (2011).
- ¹¹N. Bateman, P. Sullivan, C. Reichel, J. Benick, and M. Hermle, *Energy Procedia* (Elsevier Ltd, 2011), pp. 509–514.
- ¹²A. Siddiqui, G. Bektaş, H. Nasser, R. Turan, and M. Usman, Impact of ion implantation and annealing parameters on bifacial PERC and PERT solar cell performance, *Sustainable Energy Technologies and Assessments* **53**, 102583 (2022).
- ¹³T. Überg Nærland, H. Angelskár, and E. Stensrud Marstein, *J. Appl. Phys.* **113**, 193707 (2013).
- ¹⁴T. Niewelt, J. Schon, W. Warta, S. W. Glunz, and M. C. Schubert, *IEEE J. Photovolt.* **7**, 383 (2017).
- ¹⁵C. Park, B. Kim, N. Balaji, Y. J. Lee, M. Ju, H. Lee, and J. Yi, *J. Nanosci. Nanotechnol.* **16**, 4846 (2016).
- ¹⁶K. Bothe, R. Sinton, and J. Schmidt, *Prog. Photovolt.: Res. Appl.* **13**, 287 (2005).
- ¹⁷B. J. Pawlak, T. Janssens, S. Singh, I. Kuzma-Filipek, J. Robbelein, N. E. Posthuma, J. Poortmans, F. Cristiano, and E. M. Bazizi, *Prog. Photovolt.: Res. Appl.* **20**, 106 (2012).
- ¹⁸A. Lanterne, T. Desrues, C. Lorfeuvre, M. Coig, F. Torregrosa, F. Milési, L. Roux, and S. Dubois, *Prog. Photovolt.: Res. Appl.* **27**, 1081 (2019).
- ¹⁹C. Nyamhere, A. Scheinemann, A. Schenk, A. Scheit, F. Olivie, and F. Cristiano, *J. Appl. Phys.* **118**, 184501 (2015).
- ²⁰A. Florakis, T. Janssens, E. Rosseel, B. Douhard, J. Delmotte, E. Cornagliotti, J. Poortmans, and W. Vandervorst, *Energy Procedia* **27**, 240 (2012).
- ²¹S. D. Brotherton, J. R. Ayres, J. B. Clegg, and J. P. Gowers, *J. Electron. Mater.* **18**, 173 (1989).
- ²²K. R. C. Mok, R. C. G. Naber, and L. K. Nanver, *AIP Conf. Proc.* **1496**, 245–248 (2012).
- ²³M. Raghuwanshi, A. Lanterne, J. le Perche, P. Pareige, E. Cadel, S. Gall, and S. Duguay, *Prog. Photovolt.: Res. Appl.* **23**, 1724 (2015).
- ²⁴J. Liu and K. S. Jones, “Defect and diffusion study in boron-implanted silicon,” Thesis, University of Florida, 1996, p. 173; available at <https://www.proquest.com/dissertations-theses/defect-diffusion-study-boron-implanted-silicon/docview/304285936/se-2>.
- ²⁵D. J. Stowe, An investigation of efficient room temperature luminescence from silicon which contains dislocations, Ph.D. thesis, University of Oxford, 2016; available at <https://ora.ox.ac.uk/objects/uuid:9ee073b7-9e3c-4637-9cel-62e9e4ade69d>.
- ²⁶J. P. Goss, P. R. Briddon, T. A. G. Ebertein, R. Jones, N. Pinho, A. T. Blumenau, and S. Öberg, *Appl. Phys. Lett.* **85**, 4633 (2004).
- ²⁷J. L. Benton, S. Libertino, P. Kringhøj, D. J. Eaglesham, J. M. Poate, and S. Coffa, *J. Appl. Phys.* **82**, 120 (1997).
- ²⁸S. Libertino, S. Coffa, and J. L. Benton, *Phys. Rev. B* **63**, 195206 (2001).
- ²⁹M. Seibt, R. Khalil, V. Kveder, and W. Schröter, *Appl. Phys. A* **96**, 235 (2009).
- ³⁰J. Krugener, R. Peibst, W. Alexander, E. Bugiel, T. Ohrdes, F. Kiefer, C. Schöllhorn, A. Grohe, R. Brendel, and H. J. Osten, *IEEE J. Photovolt.* **5**, 166 (2015).
- ³¹J. Krügener, F. Wolf, R. Peibst, F. Kiefer, C. Schöllhorn, A. Grohe, R. Brendel, and H. J. Osten, in *23rd International Photovoltaic Science and Engineering Conference (PVSEC, 2013)*.
- ³²W. Shockley and W. T. Read, Jr., *Phys. Rev.* **87**, 835 (1952).
- ³³R. N. Hall, *Phys. Rev.* **87**, 387 (1952).
- ³⁴Synopsys, Sentaurus™ Process User Guide, version N-2017.09, 2017.
- ³⁵G. Hobler and S. Selberherr, *IEEE Trans. Comput.-Aided Des. Integr. Circuits Syst.* **7**, 174 (1988).
- ³⁶F. A. Wolf, A. Martinez-Limia, D. Stichtenoth, and P. Pichler, *IEEE J. Photovolt.* **4**, 851 (2014).
- ³⁷N. Zographos, *MRS Proc.* **994**, 09941001 (2007).
- ³⁸Y.-S. Oh and D. E. Ward, in *International Electron Devices Meeting 1998. Technical Digest (Cat. No.98CH36217)* (IEEE, 1998), pp. 509–512.
- ³⁹F. Lau, L. Mader, C. Mazure, C. Werner, and M. Orlowski, *Appl. Phys. A* **49**, 671 (1989).
- ⁴⁰Synopsys, Sentaurus™ Device User Guide, version N-2017.09, 2017.
- ⁴¹D. Yan and A. Cuevas, *J. Appl. Phys.* **114**, 044508 (2013).
- ⁴²D. Yan and A. Cuevas, *J. Appl. Phys.* **116**, 194505 (2014).
- ⁴³K. R. McIntosh and P. P. Altermatt, in *2010 35th IEEE Photovoltaic Specialists Conference* (IEEE, 2010), pp. 2188–2193.
- ⁴⁴H. MacKell and K. Varner, *Prog. Photovolt.: Res. Appl.* **21**, 850 (2013).
- ⁴⁵H. Haug, A. Kimmerle, J. Greulich, A. Wolf, and E. Stensrud Marstein, *Sol. Energy Mater. Sol. Cells* **131**, 30 (2014).
- ⁴⁶A. Florakis, W. Vandervorst, T. Janssens, E. Rosseel, B. Douhard, J. Delmotte, E. Cornagliotti, K. Baert, N. Posthuma, and J. Poortmans, *AIP Conf. Proc.* **1496**, 206–211 (2012).
- ⁴⁷H. Huang, L. Wang, L. Mandrell, C. Modanese, S. Sun, J. Wang, A. Wang, J. Zhao, B. Adibi, and H. Savin, *Phys. Status Solidi A* **216**, 1800414 (2019).
- ⁴⁸J. G. Fossum, R. P. Mertens, D. S. Lee, and J. F. Nijs, *Solid-State Electron.* **26**, 569 (1983).
- ⁴⁹J. G. Fossum and D. S. Lee, *Solid-State Electron.* **25**, 741 (1982).
- ⁵⁰R. R. King and R. M. Swanson, *IEEE Trans. Electron Devices* **38**, 1399 (1991).
- ⁵¹F. A. Wolf, “Modeling of annealing processes for ion-implanted single-crystalline silicon solar cells,” Doctoral thesis, Friedrich-Alexander-Universität Erlangen-Nürnberg, 2014, p. 176; available at <urn:nbn:de:bvb:29-opus4-49068>.
- ⁵²V. Kveder, M. Kittler, and W. Schröter, *Phys. Rev. B* **63**, 115208 (2001).
- ⁵³S. M. Myers, M. Seibt, and W. Schröter, *J. Appl. Phys.* **88**, 3795 (2000).
- ⁵⁴M. Seibt, V. Kveder, W. Schröter, and O. Voß, *Phys. Status Solidi A* **202**, 911–920 (2005).
- ⁵⁵R. M. Swanson, *Prog. Photovolt.: Res. Appl.* **14**, 443 (2006).
- ⁵⁶C. Donolato, *J. Appl. Phys.* **84**, 2656 (1998).
- ⁵⁷K. Ryoo, R. Drosd, and W. Wood, *J. Electrochem. Soc.* **136**, 768 (1989).
- ⁵⁸I. W. Wu, R. T. Fulks, and J. C. Mikkelsen, *J. Appl. Phys.* **60**, 2422 (1986).
- ⁵⁹D. H. Macdonald, H. Maeckel, S. Doshi, W. Brendle, A. Cuevas, J. S. Williams, and M. J. Conway, *Appl. Phys. Lett.* **82**, 2987 (2003).
- ⁶⁰D. Macdonald, P. N. K. Deenapanray, and S. Diez, *J. Appl. Phys.* **96**, 3687 (2004).
- ⁶¹J. R. Ayres and S. D. Brotherton, *J. Appl. Phys.* **71**, 2702 (1992).

- ⁶²J. R. Ayres, S. D. Brotherton, J. M. Shannon, and J. Politiek, *Appl. Phys. Lett.* **57**, 2214 (1990).
- ⁶³P. Deák, A. Gali, A. Sólyom, A. Buruzs, and T. Frauenheim, *J. Phys.: Condens. Matter* **17**, S2141 (2005).
- ⁶⁴C. Nyamhere, F. Cristiano, F. Olivie, E. Bedel-Pereira, J. Boucher, Z. Essa, D. Bolze, and Y. Yamamoto, *AIP Conf. Proc.* **1496**, 171 (2012).
- ⁶⁵D. Ding, G. Lu, Z. Li, Y. Zhang, and W. Shen, *Solar Energy* **193**, 494 (2019).
- ⁶⁶R. Peibst, U. Römer, Y. Larionova, M. Rienäcker, A. Merkle, N. Folchert, S. Reiter, M. Turcu, B. Min, J. Krügener, D. Tetzlaff, E. Bugiel, T. Wietler, and R. Brendel, *Sol. Energy Mater. Sol. Cells* **158**, 60 (2016).
- ⁶⁷F. Feldmann, G. Nogay, P. Löper, D. L. Young, B. G. Lee, P. Stradins, M. Hermle, and S. W. Glunz, *Sol. Energy Mater. Sol. Cells* **178**, 15 (2018).
- ⁶⁸F. Feldmann, G. Nogay, J. I. Polzin, B. Steinhauser, A. Richter, A. Fell, C. Schmiga, M. Hermle, and S. W. Glunz, *IEEE J. Photovolt.* **8**, 1503 (2018).